Climate Dynamics
https://doi.org/10.1007/s00382-022-06266-5

Regional climate modeling to understand Tibetan heating remote impacts on East China precipitation

Haoran Xu[1,2] · Xin-Zhong Liang[2,3] · Yongkang Xue[4]

Received: 13 September 2021 / Accepted: 14 March 2022

Abstract
The Tibetan Plateau, as a major elevated heat source, plays a critical role in the Asian monsoon and global climate. Observational data revealed significant correlations between spring surface air temperature in the Tibetan Plateau and downstream summer precipitation interannual variations. Sensitivity experiments using the regional Climate-Weather Research and Forecasting model (CWRF) were conducted to understand the physical processes and mechanisms underlying such delayed teleconnections. A positive temperature forcing was imposed over the plateau on the surface and subsurface soil layers only at the initial conditions around May 1st, 2003. This regional forcing quickly induces positive perturbations in local air temperature and, more importantly, maintains its signal in local soil, especially deep layers, for several months. Consequently, the soil temperature serves as a charged capacitor to modulate the planetary atmospheric circulation and through Rossby wave chains to cause significant summer precipitation anomalies over broad regions. This relayed teleconnection pattern is consistent with that identified from observational data records and CWRF climate simulations during 1980–2015. Diagnostic analyses of observations and simulations suggest that the Tibetan Plateau heating significantly impacts summer East Asian monsoon climate through influencing the South Asian High and shifting the East Asian jet.

1 Introduction

The Tibetan Plateau (TP), as the highest land on the earth, plays an important role in the Eurasian climate and global circulation. In particular, its complex impacts on East China precipitation associated with the East Asian Monsoon have been long documented (Ye 1981; Ding 1992; Wan et al. 2017; Zhao et al. 2018). The intensity and frequency of climate disasters have increased since 1950 in these main humid and populated regions, causing huge agricultural and socioeconomic losses every year (Huang et al. 2007; Zhang and Zhou 2015; Riyu 2000; Gao and Yang 2009). Despite long-term and extensive research, the precise scope and physical mechanism of the TP influence are still largely unknown due to the complexity of topography-atmospheric flow interaction and the lack of long, comprehensive observations.

Early studies mainly focused on the TP impact through mechanical forcing by the vast complex of high mountains on large-scale circulations. TP blocks the prevailing upper westerly jet and splits it into northern and southern airflows circumventing the plateau. This not only expands the meridional range of the jet influence but also alters the water vapor transport from the Bay of Bengal to East China (Hoskins and Karoly 1981; Chen and Trenberth 1988). As the core of the upper-tropospheric westerlies shifts to the north of the plateau, the Mei-Yu along the middle-lower reach of the Yangtze River associated with the Southeast monsoon terminates (Zeng et al. 1988; Kong and Chiang 2020). TP also blocks the South Asian Monsoon to divide unique climate characteristics between the south and north of the plateau and surrounding areas (Ding et al. 2017). This blocking effect gradually disappears as the westerly jet moves northward in summer.

Increasingly more studies emphasized the TP impact through thermal forcing as an elevated heat source in

✉ Xin-Zhong Liang
xliang@umd.edu

1 Climate, Environment and Sustainability Center, Nanjing University of Information Science and Technology, Nanjing, China

2 Earth System Science Interdisciplinary Center, University of Maryland, College Park, MD, USA

3 Department of Atmospheric and Oceanic Science, University of Maryland, College Park, MD, USA

4 Department of Geography, University of California, Los Angeles, CA, USA

Published online: 07 April 2022

summer and sink in winter (Ye 1981; Yanai et al. 1992; Wu et al. 2014). The most relevant circulation feature is the South Asian High (SAH), which is formed and maintained by the TP thermal forcing. As the most powerful thermal high-pressure system over Asia in summer, SAH has a key climatological characteristic of periodic east–west oscillations, discovered several decades ago (Tao and Zhu 1964; Luo et al. 1982). Extensive studies based on observations, reanalyses and model simulations demonstrated that interannual variations in the intensity of SAH and the location of its center have important implications for the onset of the East Asian Monsoon and regional climate (Zhang et al. 2005; Liu et al. 2013; Ren et al. 2015; Wei et al. 2015). Meanwhile, the TP thermal forcing can affect climate in a long time and a wide spatial range, and even regulate the establishment of the East Asian Summer monsoon (Wu 1984; He et al. 1987; Ueda and Yasunari 1998; Hsu and Liu 2003; Wu et al. 2014). For example, it can act as an intermediate bridge in the summer connection between the North Atlantic Oscillation and East China precipitation (Wang et al. 2018).

Several correlation analyses based on observations and model simulations showed that snow cover is an important factor in the TP thermal forcing on summer monsoon precipitation in India and East China. However, controversy still exists about its influence and mechanism at varying scales (Liang et al. 1995; Qian et al. 2003; Li et al. 2018; You et al. 2020). Some studies attributed this snow effect to the changed surface energy budget due to increasing surface albedo, while others suggested that soil moisture is the bridge between snow cover and the TP thermal forcing (Liu and Yanai 2002; Wu and Qian 2003; Zhang et al. 2004; Liu et al. 2004; Seol and Hong 2009; Xiao and Duan 2016). Nevertheless, it is consistent that the snow effect may only last from late spring to early summer due to the relatively short memory of soil moisture (Liu et al. 2004; Zhao et al. 2007; Xiao and Duan 2016).

This study presents a new idea on the TP spring heating effect and its mechanism linking to East China summer rainfall. Unlike soil moisture, soil enthalpy anomalies may persist for a long time, up to three months (Hu and Feng 2004; Yang and Zhang 2015). Temperature anomalies in surface and subsurface layers caused by snow variations or other factors over major plateaus in North America and East Asia may remain in the soil memory to produce regional climate impacts in longer times than previously thought (Xue et al. 2012, 2018, 2021). We first analyzed the observed teleconnection between TP surface air temperature and downstream precipitation and evaluate the ability of the regional Climate-Weather Research and Forecasting model (CWRF; Liang et al. 2012, 2018) in capturing this relationship. We then conducted CWRF ensemble sensitivity experiments to explore the role and mechanism of soil temperature on the teleconnection. Section 2 introduces the observational data and teleconnection pattern analysis. Section 3 describes the CWRF model configuration and performance. Section 4 presents the CWRF sensitivity experiment design. Section 5 examines CWRF's ability in capturing the observed teleconnection and compares its sensitivity experiment results to explore the underlying mechanism. Section 6 concludes with the main findings.

2 Observational data and teleconnection pattern analysis

Long-term observational data for surface and soil temperatures are rarely available in TP. The 2-m air temperature was used here as a proxy to determine the TP remote impact on China precipitation given its close correlation with surface (skin) temperature and better observational availability. Both air temperature and precipitation observations were taken from the China meteorological forcing dataset that integrated remote sensing products, reanalyses, and in-situ measurements at monitoring stations (He et al. 2020). The dataset is available at a horizontal grid of $0.1° \times 0.1°$ and a 3 hourly interval covering the period of 1979–2018.

This study used a singular value decomposition (SVD) analysis to identify the observed teleconnection between TP air temperature and downstream precipitation anomalies during 1980–2018. SVD is an effective diagnostic method to extract the leading pairs of spatially orthonormal patterns that explain as much as possible the mean-squared temporal covariance between two variables (Bretherton et al. 1992). The two variables are referred to as the left and right fields in the SVD decomposition. Each SVD mode consists of paired left- and right-singular vectors of spatial patterns along with their respective time series of expansion coefficients. The geographic distribution of temporal correlations between an input field and a SVD expansion coefficient represents a remote connection pattern. Homogenous correlations show remote connections within a field and are calculated by correlating the input field with its own expansion coefficient (e.g., all left or all right). Conversely, heterogeneous correlations represent teleconnections between the fields and are calculated between a field and the other field's expansion coefficient. This study focused on the heterogeneous correlation patterns.

Table 1 lists the temporal correlations between time series of the expansion coefficients of spring (March–May) air temperature over TP and March to August precipitation in East China for the first SVD mode at different monthly lags (0–3) and with summer mean. It also lists the percentage of the spatial covariance explained by this mode for each lag pair. All the modes had dominant variance contributions, with the percentage ranging from 39.5 to 65.3%. Temperatures in March, April and May all had significantly ($p < 0.01$) high

Table 1 The temporal correlations between the time series of the expansion coefficients of spring (March to May) air temperature and subsequent (March to August and Summer) precipitation for the first SVD mode at different monthly lags

PRA / T2M	March	April	May	June	July	August	Summer (JJA)
March	0.74 (55.7%)	0.67 (48.4%)	0.63 (65.3%)	0.79 (44.2%)	0.84 (47.9%)	0.72 (47.5%)	0.76 (40.6%)
April		0.71 (59.6%)	0.65 (63.6%)	0.64 (59.5%)	0.72 (46.1%)	0.81 (45.7%)	0.74 (47.0%)
May			0.74 (42.2%)	0.73 (40.0%)	0.67 (39.5%)	0.77 (41.9%)	0.69 (42.5%)

The percentage of the spatial covariance explained by this mode is shown in the parentheses

correlations with precipitation in the same and subsequent several months. For example, May temperature had a lag correlation (0.73) with June precipitation. This delayed temperature effect on precipitation persisted into August, having their correlation (0.77) even larger than other lags. These spring monthly temperature anomalies (March, April, May) over TP were strongly associated with summer precipitation patterns in East China, respectively having correlations of 0.76, 0.74, 0.69 and capturing 40.6%, 47.0%, 42.5% of the total covariance, respectively. To follow the protocol of the experiment design for Impact of Initialized Land Surface Temperature and Snowpack on Subseasonal to Seasonal Prediction Project Phase I (LS4P-I, Xue et al. 2021), this study defines the Tibetan heating as a temperature anomaly in May over TP and focuses on its impacts during summer.

Figure 1 shows the coupled spatial patterns (heterogeneous correlation) of the first SVD mode between May temperature and summer precipitation. Negative temperature anomalies extended over most of TP and corresponded with precipitation positive anomalies in the Northeast and negative anomalies along the Yellow River middle to lower reaches, Shandong Peninsula, and northern Inner Mongolia as well as south of the Yangtze River middle to lower reaches. These areas of significant precipitation anomalies were coincident with the prevailing rainbands associated with the summer monsoon system in East China. The time series of the expansion coefficients for the coupled patterns varied largely among years but consistently between the two fields (Fig. 1c). The coupled patterns were typical of the delayed relationships between spring temperature and summer precipitation. For all lags in Table 1, the temperature patterns were characterized by dominant homogeneous anomalies over TP, whereas the corresponding monthly precipitation patterns exhibited major signals in East China with large variations in the sign and magnitude of regional anomalies (Fig. S1).

The above observed SVD analysis indicated significant teleconnections between spring Tibetan heating and downstream summer precipitation. However, lacking soil surface and subsurface data over TP renders it difficult to both determine the source of the heating and understand the physical processes and underlying mechanisms. This study seeks numerical simulations to first reproduce the observed patterns and then explore the mechanisms. To facilitate the study, the summer of 2003 was selected when severe droughts occurred in the southern part of East China and flooding in the northern part (Fig. 2b), resulting in great agricultural and socioeconomic losses (Zhang and Zhou 2015; Seol and Hong 2009). Meanwhile, almost the entire TP region experienced a cold spring, with an average anomaly of -2.0℃ (Fig. 2a). These significant anomalies observed in the summer of 2003 resembled the first SVD coupled mode of interannual variations during 1980–2018 (Fig. 1), although the negative (positive) precipitation anomalies north of the Yellow (Yangtze) River were weaker (stronger). In addition, surface air temperature anomalies in East China were positive in the South and North-Northeast but negative in the Central and the northern border.

3 CWRF description and performance

The CWRF has been developed and continuously updated as a Climate extension of the Weather Research and Forecasting model (WRF, Skamarock et al. 2008) by incorporating substantial improvements in representing key physical processes and their interactions as well as surface and lateral boundary conditions, all of which are essential to climate modeling (Liang, et al. 2012, 2018; Liang and Zhang 2013; Zhang et al. 2013; Choi et al. 2013; Xu et al. 2014; Ling et al. 2015; Qiao and Liang 2015, 2016, 2017; Sun et al. 2020a,b). It has been widely applied in the United States and China, achieving superior performance, especially for precipitation and extremes (Yuan and Liang 2011a; Liang et al. 2012, 2018; Chen et al. 2016; Liu et al. 2016; Li et al. 2020; Sun et al. 2020a,b; Jiang et al. 2021).

Most relevant to this study is the state-of-the-art conjunctive surface–subsurface process (CSSP) model built-in CWRF (Choi et al. 2007, 2013; Choi and Liang 2010; Yuan and Liang 2011b). The CSSP not only predicts soil moisture vertical transport and exchange with the atmosphere as in typical land surface models but also uniquely represents

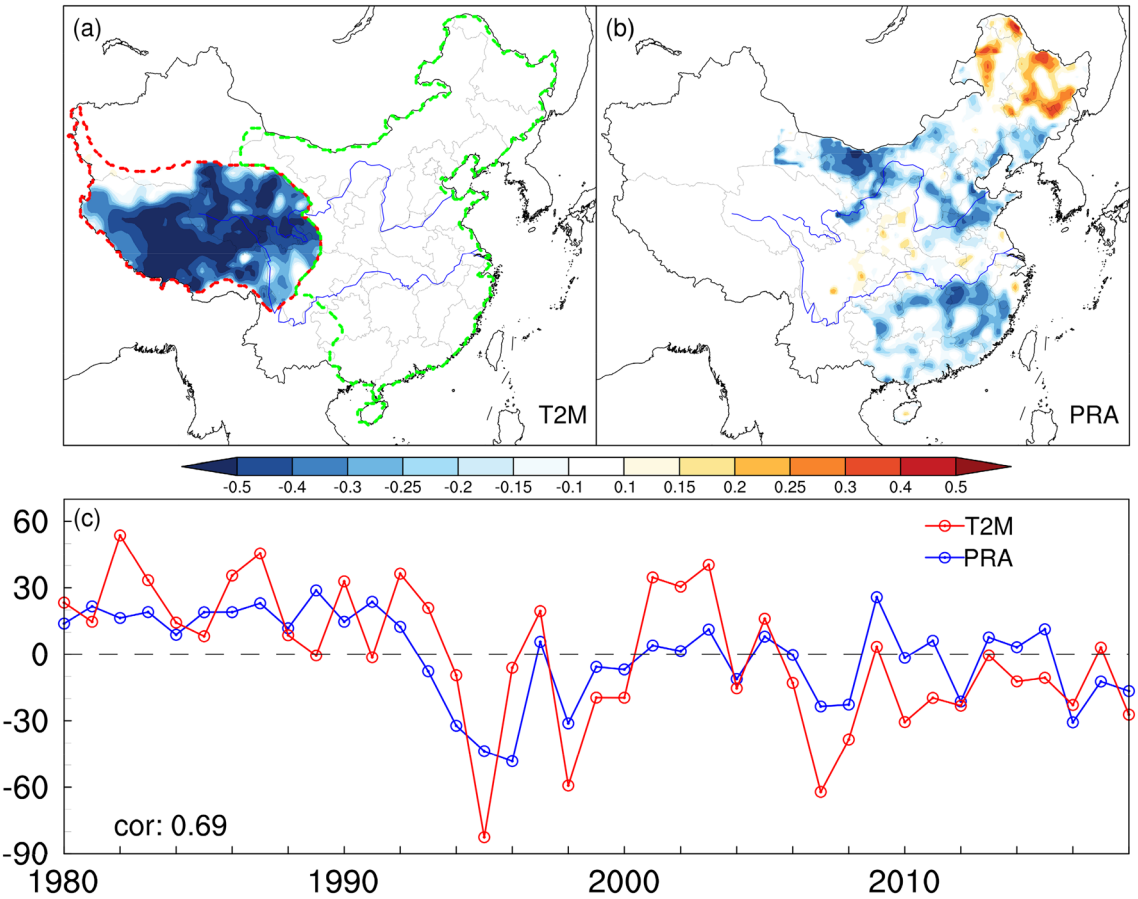

Fig. 1 The coupled spatial patterns of the first SVD mode for **a** May air temperature with the key signals over TP (within the red dashed line, terrain height above 4000 m) and **b** summer precipitation with the key signals over eastern China (within the green dashed line in a) as well as **c** the time series of their respective expansion coefficients. This mode explains 42.5% of the spatial covariance between the two fields with a temporal correlation of 0.69 between their expansion coefficients

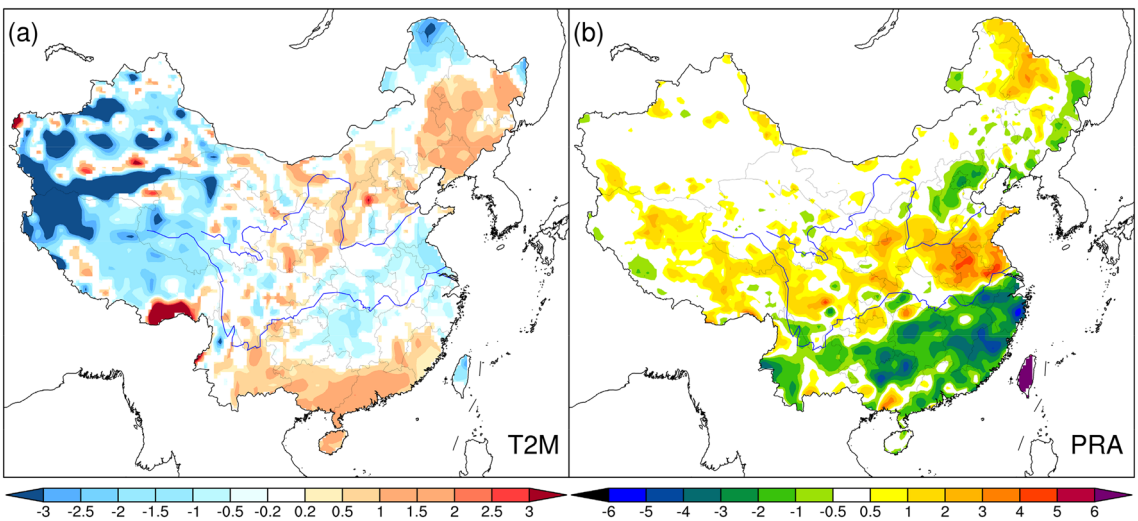

Fig. 2 Observed **a** May temperature (ºC) and **b** summer precipitation (mm day^{-1}) anomalies in 2003

the 3-D lateral flow and subgrid topography-controlled soil moisture transport that interact with the surface routing and subsurface horizontal water movement. Along with the realistic treatment of surface boundary conditions such as topography, soil, and vegetation distributions (Liang et al. 2005a; Xu et al. 2014) and the advanced dynamic-statistical parameterization of land surface albedo (Liang et al. 2005b), CSSP accurately represents the terrestrial hydrological processes and their impacts on regional climate (Liang et al. 2012). Its applications are growing (Gan et al. 2015; Ji et al. 2017; Yuan et al. 2018). The CSSP's comprehensive subsurface treatment facilitates our quantification of the Tibetan heating source and subsequent impact.

This study used the CWRF computational domain following Liu et al. (2008), with the center at (35.18° N, 110.0° E) on the Lambert conformal map projection and a horizontal spacing of 30 km for a total of 232 × 172 grids. The model contained 36 vertical terrain-following sigma (σ) levels with the top at 50 hPa and selected the following physics configuration: cumulus—ECP penetrative convection (Liang et al. 2004a; Qiao and Liang 2015, 2016, 2017) plus UW shallow convection (Bretherton and Park 2009), microphysics—GSFCGCE (Tao et al. 2003), cloud—XRL (Xu and Randall 1996; Liang et al. 2004b), aerosol—MISR (Kahn et al. 2005), radiation—GSFCLXZ (Chou and Suarez 1999; Chou et al. 2001), planetary boundary layer—CAM (Holtslag and Boville 1993) plus ORO (Rontu 2006; Liang et al. 2006), and Surface—CSSP land with 11 soil layers up to 5.7 m depth (see above for references) plus UOM ocean of 30 layers up to 300 m depth (Ling et al. 2015). This CWRF configuration has been well evaluated to realistically capture regional climate variations in China (Liang et al. 2018; Li et al. 2020; Xu et al. 2021; Shi et al. 2021; Wei et al. 2021; Jiang et al. 2021).

For all CWRF simulations in this study, the initial and lateral boundary conditions were based on the 6-hourly ECMWF-Interim reanalysis data at ~ 80 km horizontal grid spacing (ERA-interim, Dee et al. 2011). Daily sea surface temperature distributions were derived from NOAA OISST analysis at 0.25° (Reynolds et al. 2007; Banzon et al. 2016) and used in UOM for relaxation to minimize the model prediction drift due to the lack of the deep and global ocean dynamics (Ling et al. 2011, 2015).

Figure 3 shows the May temperature and summer precipitation anomalies in 2003 simulated by CWRF from its continuous integration of 36 years (1980–2015) driven by ERA-interim. As compared with observations in Fig. 2, CWRF realistically reproduced these anomalies over most regions with finer structures. Obvious and realistic temperature signals included the cold anomalies over TP and Xinjiang and the warm-cold-warm anomaly pattern in East China. The model biases from observations were generally small (Fig. 3c). Temperature biases were within 1° over most China land except for small parts of TP and northeastern mountains up to 2°. Correspondingly, CWRF well captured the precipitation anomaly patterns, having droughts in the Southeast and heavier than normal rainfall in the North, albeit the boundaries were shifted northward, especially for the northern parts. Most global and regional climate models, however, could not fully produce these 2003 anomalies (Xue et al. 2021). It is very encouraging that CWRF in a free run without perturbation was able to reproduce the major anomalies. Therefore, CWRF is credible to use for understanding the Tibetan heating impact on East China precipitation.

4 Sensitivity experiment design

Systematic TP cold biases were found in modern reanalyses and current global climate models, some reaching 7 °C (Frauenfeld et al. 2005; Xie et al. 2007; Wang and Zeng 2012; You et al. 2013, 2016; Zhu and Yang 2020; Xu et al. 2021). Although overall model advances over a decade reduced the biases (Zhu and Yang 2020), resolution increases did not help much (Xu et al. 2021). On the other hand, CWRF downscaling with more advanced physics significantly improved the TP simulation of both its climate and interannual variation (Xu et al. 2021). Nonetheless, all models still contain large departures from very limited observations over TP. These departures, whether due to observational uncertainty or model deficiency, are simply referred to as model biases here. On average over TP, CWRF produced a cold bias of 1.5 °C in May 2003 (Fig. 3c). Below CWRF sensitivity experiments were designed to explore how a correction for such TP cold biases in spring induce summer teleconnection precipitation anomalies in East China.

Previous studies have shown that the near-surface forcing would dissipate rapidly (in a couple of days) if only surface air and land skin temperature perturbations were imposed to initial conditions. The only way for climate models to memorize the signal and produce significant feedback is to impose the forcing on both surface and subsurface soil temperatures (Xue et al. 2012, 2018). However, most models still failed to fully capture the delayed teleconnection patterns (Xue et al. 2021). Fortunately, CWRF captured the key climate anomalies driven by lateral boundary conditions alone (Fig. 3a–c), although some modest cold biases still existed over TP. This study adopted the initialization approach proposed by Xue et al. (2021), that is, imposing positive perturbations on both surface and subsurface temperature initial conditions over TP to offset the model drift and so eliminate local cold biases. Given the surface air temperature monthly mean anomaly observed (T_{anomaly}) and bias

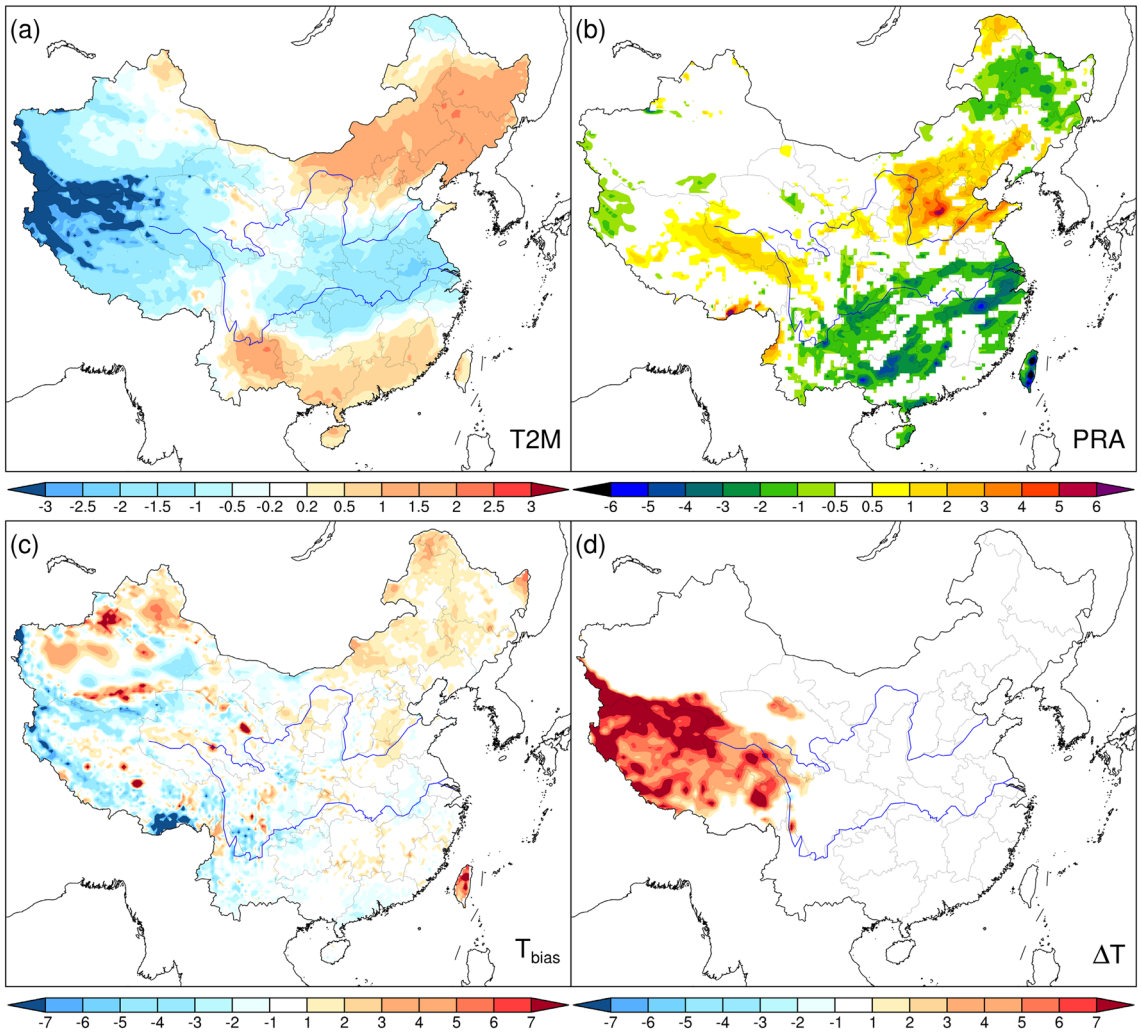

Fig. 3 CWRF simulated **a** May temperature (ºC) and **b** summer precipitation (mm day^{-1}) anomalies in 2003. **c** CWRF May temperature bias (ºC) from observations. **d** Imposed land surface and subsurface temperature perturbation (ΔT, ºC) over the Tibetan Plateau at the initial step of the sensitivity experiments

modeled (T_{bias}), the initial temperature forcing at each grid over TP was defined as:

$$\Delta T = -n \times T_{\text{anomaly}} - T_{\text{bias}}$$

where n is a tuning parameter to compensate for the general soil memory loss by land models. Based on previous studies (Xue et al. 2012, 2018) and combined with our CWRF test runs, $n = 2$ was chosen for this study. Figure 3d shows the distribution of the forcing that was imposed at the initial step to the ground (skin) and all 11 soil layers' temperature in CSSP.

A CWRF run could be started directly from the ERA-interim driving conditions or restarted at any given time from its own long continuous integration driven by ERA-interim, called respectively a cold or warm start. A cold start inputs only the basic atmosphere (temperature, wind, humidity) and surface (snow, vegetation, soil temperature/moisture) conditions from ERA-interim, while artificially setting other variables like cloud hydrometeors. Given large dynamic and physical formulation differences between CWRF and ERA-interim, these atmosphere and surface states are not balanced nor consistent for the coupled CWRF/CSSP system and thus may drift away after a spin-up period. In contrast, a warm start begins with a balanced and consistent state of the system itself. In either case, this study perturbed the start state by adding the initial forcing ΔT to temperatures at the surface and all subsurface soil layers. Such a perturbation alone may cause an unbalanced state unless soil moisture is also consistently set. This is particularly important because a soil temperature change may alter the soil water phase from liquid to ice or vice versa, which is associated with a huge latent heat difference.

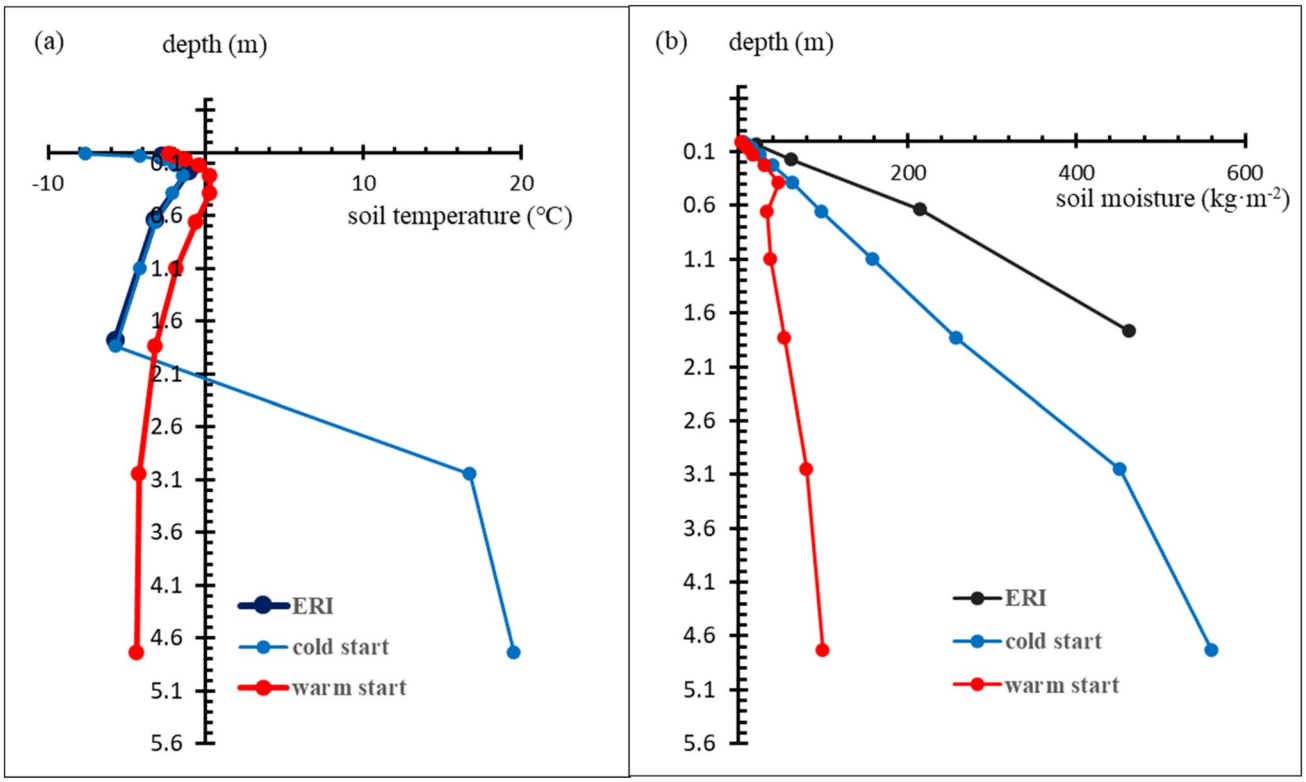

Fig. 4 Initial conditions on May 1st of 2003 from ERI data and CWRF cold and warm start for **a** soil temperature (ºC) and **b** soil moisture (kg m^{-2})

Figure 4 compares the soil temperature and moisture profiles averaged over TP on 1 May 2003 as derived from ERA-interim and CWRF cold and warm start initial conditions. ERA-interim produced systematically colder soil temperatures than the control CWRF long-term climate integration (see the warm start). Since ERA-interim provided soil data only up to the depth of 2.55 m and the CWRF pre-processor assigned the observed annual mean surface air temperature as the soil condition at the bottom (5.67 m), the cold start soil temperature had abrupt increases in deeper layers due to unrealistic extrapolation. On the other hand, ERA-interim simulated substantially wetter soil moisture contents than the control CWRF by several times. The warm start gave more reasonable profiles of soil temperature (warmer than ERA-interim) and moisture, which were also balanced with the atmospheric forcing as resulted from the long-term CWRF/CSSP coupling.

Based on the above discussion, this study conducted five sets of CWRF experiments. Each set consisted of 10 ensemble runs starting from 22 April to 1 May at a daily interval for an 8-month integration till 31 December 2003. All experiments were driven by the same ERA-interim 6-hourly lateral boundary conditions and OISST daily sea surface temperature distributions. Table 2 lists the experiment configurations, each defined by whether the control initial state (I) was balanced (b), the initial soil temperature (T) perturbed (p), and the initial soil water phase (W) changed as the soil temperature crossing the freezing point (c). For convenience, these configurations were referred below by abbreviations that combine the prefixes (I, T, W) each followed by the respective choice (b, p, c) or not (n). For example, InTnWn depicts that the initial state was not balanced (cold start), the soil temperature was not perturbed, and the soil water phase was not changed. Similarly, IbTpWc means that the initial state was balanced (warm start), the soil temperature perturbed, and the soil water phase changed (see below).

Table 2 Experiments design in this study

Experiment abbreviation	Control initial state (I) b = balanced, n = not	Soil temperature perturbation (T) p = perturbed, n = not	Soil water phase change (W) c = changed, n = not
InTnWn	Not (n)	Not (n)	Not (n)
InTpWn	Not (n)	Yes (p)	Not (n)
InTpWc	Not (n)	Yes (p)	Yes (c)
IbTnWn	Yes (b)	Not (n)	Not (n)
IbTpWc	Yes (b)	Yes (p)	Yes (c)

Incorporating into the initial perturbation the soil water phase change according to the soil temperature change is critical because the latent heat of melting ice is ~ 78 times the specific heat of liquid water per K. A positive perturbation may raise the soil temperature from below to above the freezing point in some grids or layers, where the local soil water, if not adjusted accordingly, would remain in the ice form. Comparison between InTnWn and InTpWn revealed that the initial temperature perturbation dissipated rapidly during the first few days, just like in other global and regional climate models (Xue et al. 2021). This occurred because the imposed temperature forcing made most grids in TP rise from below to above the freezing point and that extra heat was quickly consumed to melt the existing ice. Thus, InTpWn was discarded in the subsequent analysis. In all the experiments with initial soil temperature perturbations, the existing local ice content was fully converted into liquid water at any grid or layer if the soil was heated above the freezing point.

Note that most climate models do not explicitly predict frozen or ice soil moisture and thus may not directly encounter such water phase change issues. ERA-interim provided no soil ice content, which made the CWRF cold start even more arbitrary as soil temperature crossed the freezing point. Ideally, a spin-up for decades is needed for a model to reach an equilibrium state where soil temperature and moisture in both liquid and ice phases are fully balanced with each other as well as with the atmosphere (Liu et al. 2020). Nonetheless, the warm start from the control CWRF's 36-years (1980–2015) continuous integration offered a more realistic initial state than the cold start.

5 Results and discussion

Below the analyses focused on the differences between the CWRF sensitivity and control experiments to quantify the Tibetan heating impacts. All results were shown as the ensemble mean of the 10 realizations differing only in the start date, and those passed the t test at the 95% confidence level were considered as statistically significant signals.

Figure 5 shows May–August monthly mean distributions of surface air temperature and precipitation differences between the cold start InTpWc and InTnWn. These differences depict the local and remote impacts of the initial temperature perturbation with corresponding water phase change imposed to the surface and subsurface soil layers over TP. As reflected in surface air temperature, the local signal was robust and persisted for about five months. On average over TP, May–August monthly mean temperatures were increased by 0.68, 0.54, 0.47, and 0.17 ℃, respectively. Considering that the TP forcing was more than 5 ℃ at the initial step, the warming averaged in the first month was rather weak, implying a large energy loss during the spin-up to gain the surface-atmosphere balance through ground longwave emission and sensible heat. Nonetheless, the result demonstrated that CWRF could retain a portion of the initial forcing to reduce the systematic cold bias in the May air temperature anomaly by almost half (− 0.73 versus − 1.41 ℃). Initially, the soil forcing influence was confined to TP in May and then induced a significant response in East China by altering large-scale circulation (see below). Especially, in July large cooling of 0.5–1.5 ℃ appeared in Northeast to North China, and in August this cooling expanded southward to cover North to Central China. Meanwhile, a band of heating appeared to the south of the Yangtze River, evident in July over Zhejiang-Fujian and western Yunnan and more organized in August across the divide between Central and South China.

The precipitation responses to the TP heating appeared earlier (Fig. 5b). In May, significant rainfall increases occurred over the eastern TP, a source region of the Yangtze River, together with changes of both signs over smaller areas around the middle to lower reaches of the river. In June, the signal was amplified, when rainfall increased over the eastern and southern TP and in most of the Northeast and decreased over the North and in scattered regions across the Yangtze River and the south and eastern borders of continental China. In July, the changes were more pronounced and much more organized. Large decreases (up to 7 mm day^{-1}) occurred in a long band extending from Inner Mongolia to North and Northeast China. At the same time, there were large increases (up to 7 mm day^{-1}) immediately to the south of the band, covering the broad areas across the source region of both the Yellow and Yangtze Rivers, between their middle reaches, in the Yellow River lower reach, and the Shandong Peninsula. Further south, notable decreases (up to 2 mm day^{-1}) occurred in the Sichuan Basin. This oscillating pattern indicated a systematic southward shift of the summer monsoon rainband in East China. In August, the rainband was still shifted southward. Large decreases focused across Inner Mongolia to North China, while large increases expanded over most areas between the two rivers. Further south, large decreases extended over most of the Southwest and the regions south of the Pearl River. Meanwhile, modest increases existed in the Northeast.

Figure 6 shows May to August monthly mean distributions of surface air temperature and precipitation differences between the warm start IbTpWc and IbTnWn. The TP heating was systematically weaker than the cold start. On average over TP, May–August monthly mean temperatures were increased by 0.55, 0.31, 0.18, and 0.07℃. This weakening was expected as the initial soil moisture content was several times lower in the warm than cold start so that much less latent heat was retained under the same temperature forcing. Correspondingly, the remote temperature effects of the TP

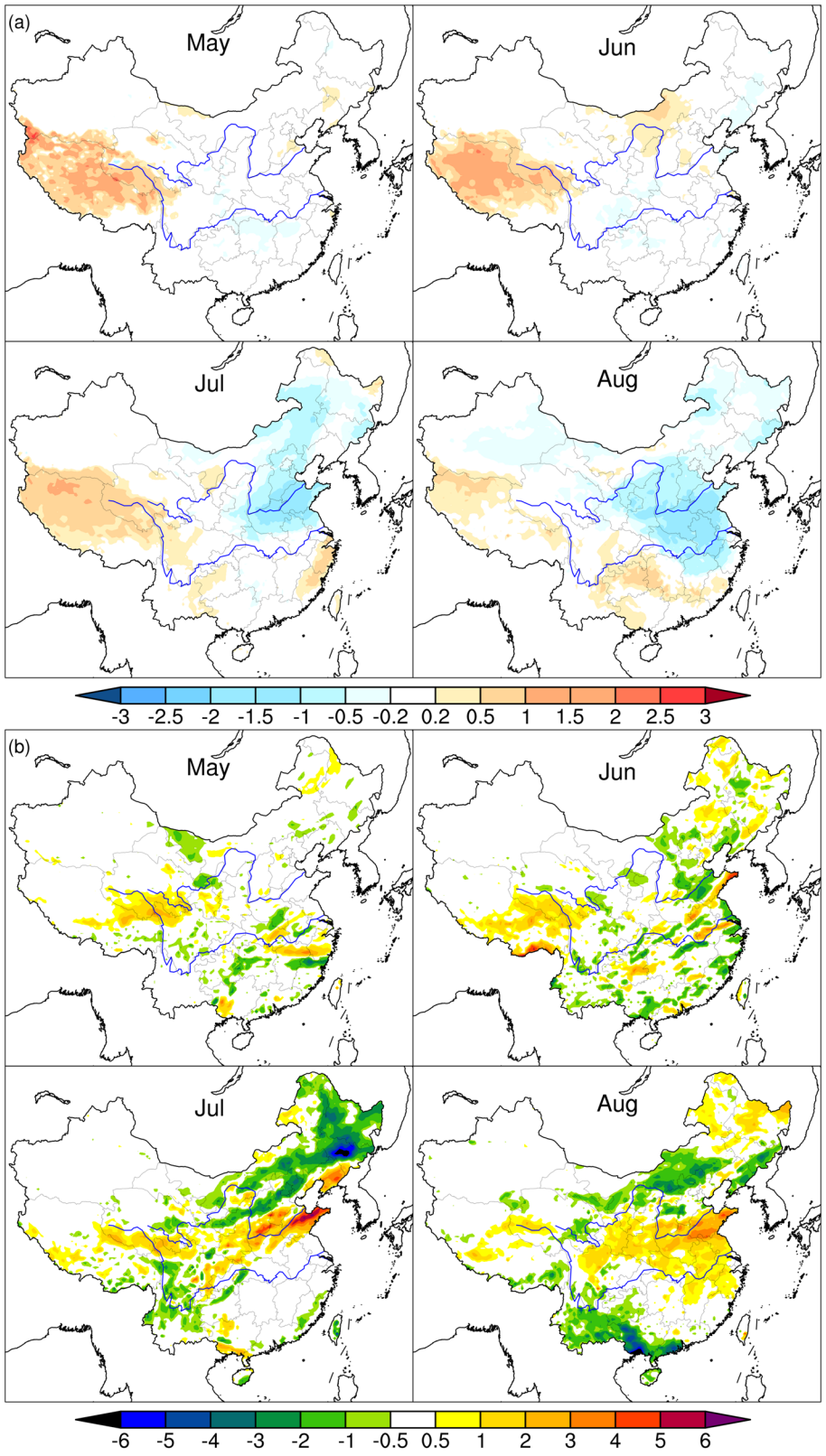

Fig. 5 CWRF simulated monthly (May–August) mean differences in **a** temperature (ºC) and **b** precipitation (mm day^{-1}) between the cold start InTpWc and InTnWn

heating were also weaker, but the spatial patterns resembled those from the cold start. One exception was in August when the strong cooling center across North to Central China from the cold start was replaced with a broad warming (0.5–1.5 ˚C) center over Central China excluding the region across Jiangsu-Zhejiang-Jiangxi. For precipitation, the

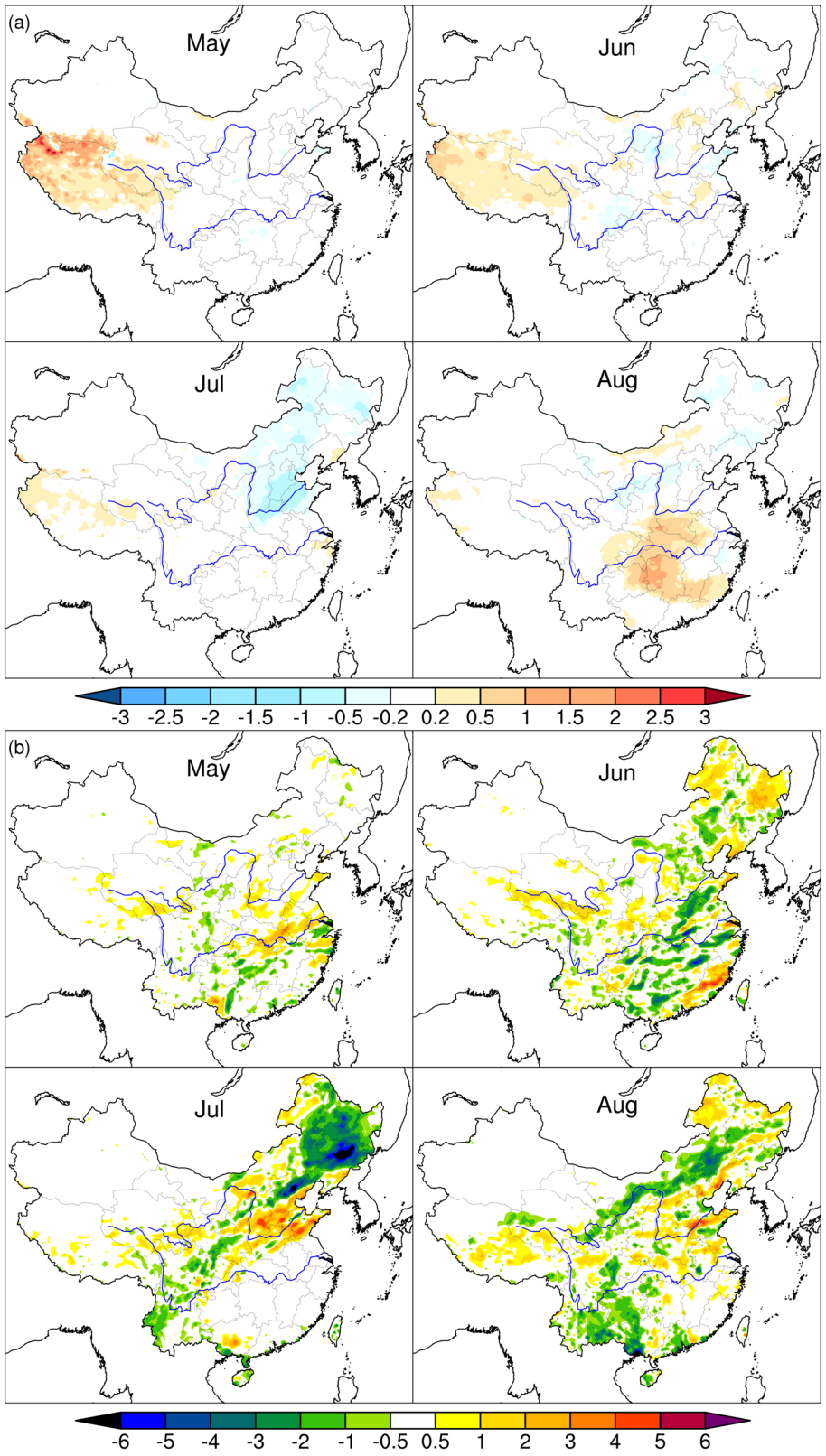

Fig. 6 CWRF simulated monthly (May–August) mean differences in **a** temperature (ºC) and **b** precipitation (mm day^{-1}) between the warm start IbTpWc and IbTnWn

responses were also generally weaker in the warm than cold start, especially over TP. On the other hand, large changes (up to 7 mm day^{-1}) of both signs were still produced over broad downstream regions. In particular, the July and August patterns resembled those from the cold start, albeit differing in regional magnitude and coverage.

Despite the response differences noted above between the cold and warm starts, the delayed precipitation teleconnection patterns in East China were highly consistent with each other and both were clearly identified with the systematic southward shift of the summer monsoon rainband. Climatologically, the rainband is characterized by a stepwise poleward advance over East China. It arrives in South China during May, advances to the Yangtze River valley in June, and establishes in North China together with another rainband in the Northeast in July (Samel et al. 1999). By early August, the summer monsoon starts to retreat southward. The TP forcing must have altered the summer monsoon circulation so to change the rainband advance and retreat processes. Subsequent analyses explored the key mechanisms underlying the delayed teleconnection from the spring heating over TP. Given that the cold start introduced excessive surface-atmosphere inconsistencies and imposed unrealistic big energy perturbations, the analyses below focused on the warm start IbTpWc minus IbTnWn differences.

The initial soil temperature represents the heating source over TP, which decays over time. The decay speed depends on soil thermal diffusivity which equals thermal conductivity divided by density and specific heat capacity at constant pressure. Given its large density and heat capacity, the soil has small diffusivity and so slow decay for its initial forcing. Thus, the soil has a long memory, a prerequisite for the TP heating to induce delayed local and remote climate responses.

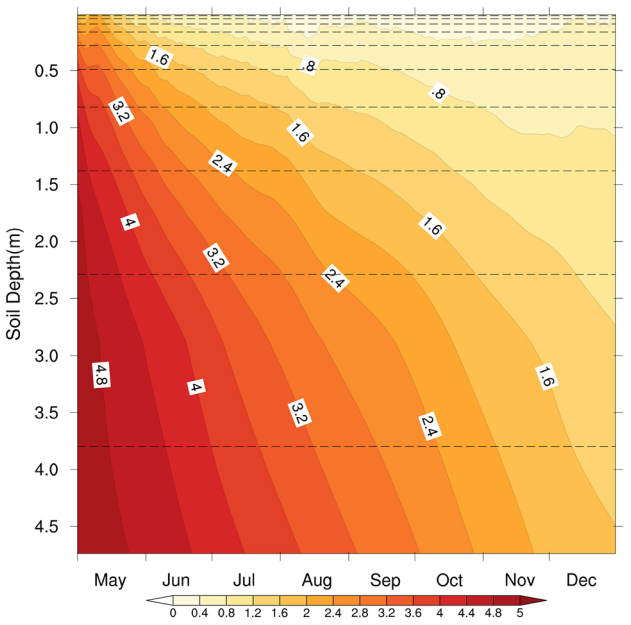

Fig. 7 Depth-time variations of the TP-averaged soil temperature differences between the warm start IbTpWc and IbTnWn. The dashed lines depict interfaces between model soil layers

Figure 7 shows the variation of daily mean soil temperature vertical profile differences averaged over TP. Initial temperature forcing is well preserved in the soil with the penetrating (to deeper layers) and decaying (in time) rates close to observations (Liu et al. 2020), indicating that CWRF/CSSP is able to reproduce this soil memory, which is difficult to do in other climate models (Xue et al. 2021). The memory increases with depth, so initial soil temperature perturbations in deeper layers decay significantly slower. In upper layers, the forcing of initially ~ 5 ℃ drops to 2 ℃ in only a few days, while the same change takes 50 days at 1-m depth and 100 days at 2-m depth. Once the soil reaches below 2 m, half of the initial forcing can be maintained for more than 2 months, from spring to summer. At the bottom of the soil, a certain amount of the forcing (~ 1 °C) persists even into the following year. The above results are consistent with the observed characteristics of soil temperature distribution, i.e., deep layer soil usually has very weak seasonal-interannual variation.

The soil temperature evolution reveals a robust energy transfer path through surface sensible and latent heat fluxes (Fig. 8). The near-surface soil layer continuously transfers sensible heat to the air (remaining significant until September), resulting in an increased soil temperature gradient between shallow and deep layers, thereby generating more heat transfer upward. This heat transfer process is slow, retaining deep layer heating for over four months. The surface warming enhances evapotranspiration as depicted by the positive latent heat difference over TP, which is generally weaker than that of the sensible heat. This increases local precipitation in the first few months (Fig. 6) but also quickly dries out soil moisture during the initial one month, although with following wetter conditions due to more precipitation (Fig. S3). Thus, the memory of soil moisture is significantly shorter (by ~ 2 months) than that of soil temperature. In addition, the warmer surface also produces larger longwave emissions. In summary, the initial TP forcing, especially in deep soil, acts as a long-term heat source, and the continued ascent of moist hot air masses enhances local convection and precipitation.

After the TP heating continues for about a month, notable changes in both sensible and latent heat fluxes appear remotely in East China. In June, larger sensible heat downstream of TP coincides with warmer air temperatures between the lower reaches of the Yangtze and Yellow Rivers, while latent heat and so rainfall changes of both signs spread across East China (Fig. 6). In July, the downstream sensible heat response is weak (with colder air temperatures shifted northward into North-Northeast China), while the latent heat and rainfall changes in East China are enhanced. In August, both increases in sensible heat and decreases in latent heat are significantly enlarged downstream of TP,

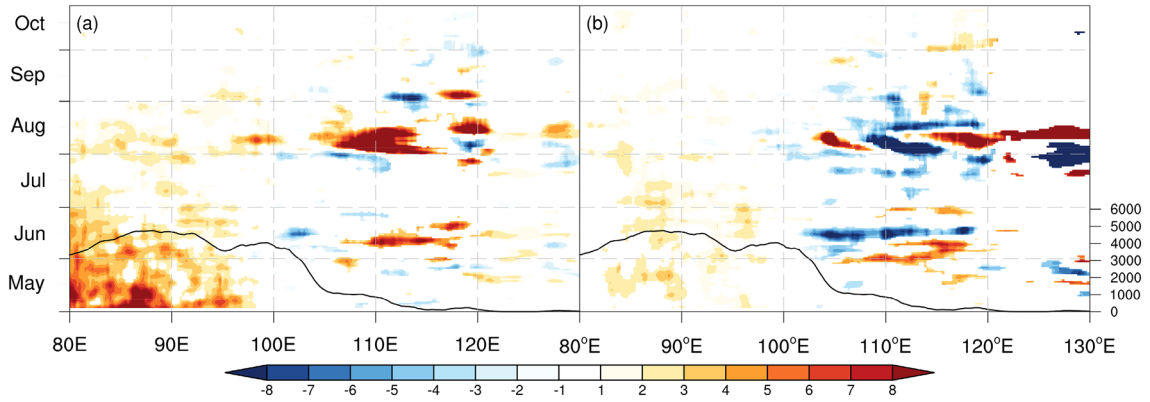

Fig. 8 CWRF simulated time-longitude variations of 27° N–37° N latitudinal mean surface **a** sensible and **b** latent heat flux (W m^{-2}) differences between the warm start IbTpWc and IbTnWn. The black lines depict the latitudinal mean terrain elevation (m), using the scale on the right

which correspond to more organized temperature and precipitation increases there. Remote signals widely spread across East China and coastal oceans in July and August. These signals are essentially produced by atmospheric perturbations induced remotely by the initial TP heating, as discussed below.

The warmer surface of TP results in a smaller air density and lower pressure in near-surface layers, causing an anomalous convergence and upward motion, which promotes stronger local turbulent mixing and a deeper, warmer planetary boundary layer (Fig. S2). Combined with the moistening from more evapotranspiration, the forced rising warmer and wetter air mass increases local precipitation. Since TP has a considerable area of elevations above 5000 m, the impact of its surface heating can be rapidly transmitted to the middle and even upper troposphere, producing geopotential height anomalies aloft.

To better understand how the TP heating effect on the atmospheric circulation evolves in space and time, we compared the day-by-day (Fig. S4) and week-by-week (Fig. S5) geopotential height results between the runs initiated on May 1. We did not use the ensemble mean of the 10 members initialized one day apart, because their cumulative 10-day span would interfere the comparison considering that the large-scale wave propagation across China may take only a few days. On the first day, the TP heating induces above a coupled 500-hPa cyclonic and 300-hPa anticyclonic circulation anomaly. The associated vorticity anomaly propagates downstream by large-scale waves, initially along the TP latitude band under the prevailing westerly flow and later spreading to northern China and Mongolia. By days 3–4, a negative 300-hPa height anomaly occurs over northeast China to southern Okhotsk Sea. This anomaly changes its sign in day 5 and reappears in days 6–7, and so on. The distance between the positive and negative anomaly centers is ~ 5000 km and the traveling speed is ~ 12 m s^{-1}, which are consistent with the characteristic wavelength and phase speed of Rossby waves. In the first week, the 300 and 500-hPa anomalies are almost opposite in sign, so to enhance baroclinicity. The circulation anomalies are continuously adjusted along with the evolving vertical motion and latent heat, and finally become quite stationary and barotropic after week 7. During the entire process of the wave activities, the boundaries between significant 300-hPa cyclonic and anticyclonic anomalies mostly overlay the exit region of the East Asian upper-level westerly jet (ULJ), around North-Northeast China. These anomalies exert important impacts on the jet location and the secondary circulation across the jet, which are essential to summer rainfall distribution in East China (Liang and Wang 1998).

The condensation latent heat and vertical energy transport by the enhanced moist convection as well as the induced stronger subsidence and adiabatic heating collaborate to produce widespread warming in the mid-upper troposphere beyond the forcing area over TP. In May, this causes a perturbed warming center at 100 hPa to the northeast of TP, covering the entire Yellow River basin, and shifts the ULJ northward (Fig. 9). The heating elevation is strengthened in June and expanded to also cover the entire Yangtze River basin, while the jet north shift continues. In July, the mean (i.e., unperturbed or IbTnWn) SAH (see the 17,700 m contour at 100 hPa) intensifies and advances northward to govern across the entire TP to Central China, while the mean ULJ (see the 25 m s^{-1} contour) jumps by ~ 10° to the north

of the June position (Fig. 9b). The TP heating now induces the warming perturbation across the SAH center latitude band from TP to Central China and coastal oceans, which is coupled with a significant cooling center over the Northeast. That cooling adds perturbed resistance to the ULJ north jump, keeping it more to the south. As a result, the Northeast to North China is under the influence of subsidence cooling air behind the ULJ's left exit and so has colder and drier surface conditions, whereas the lower reach of the Yellow River basin is affected by stronger ascending motion on the ULJ right exit and so has more precipitation (Fig. 6). In August, the mean SAH further intensifies while the mean ULJ strengthens and continues moving northward (Fig. 9). Although the SAH northern cooling (southern warming) perturbations induced by the initial TP heating largely dissipate (diminish), the ULJ exit core is enhanced and concentrated (from both north and south sides). This causes even stronger descending motions not only beneath the ULJ's left exit but also to the far-right flank, and hence results in less precipitation across Inner Mongolia to North China and warmer surface air temperature over Central China, respectively (Fig. 6).

Figure 10 shows the composite of monthly mean differences in precipitation, 850-hPa wind vector, and 200-hPa zonal wind component, whose mean value is also overlaid to depict the ULJ position. A major signal occurs in July when the mean ULJ core locates right above the Northeast and is accompanied by significant positive (negative) perturbations to its right (left) exit. This indicates the ULJ is shifted southward, which is associated with a strong low-level cyclonic circulation anomaly across the Northeast coasts, the Yellow Sea, the Korean Peninsula, the Sea of Japan, and Japan. As shown by Liang and Wang (1998), a south shift of the ULJ induces a secondary circulation across the jet exit region with upward (downward) motions to the right (left). Consequently, a pronounced cooling and drier center occurs over the Northeast, whereas a heavier rainfall center appears in North China and across the Yellow Sea, Korea to Japan (Figs. 6, 9, 10). These anomalous changes weaken in August.

Note that the changes in near-surface and shallow-soil temperatures as well as surface sensible and latent heat fluxes over TP decrease significantly after June (Figs. 7, 8). Thus, the enhanced surface air temperature and precipitation anomalies during July and August over East China (Fig. 6) may not be a direct response to the weak TP forcing that remains in these months. In addition, the lateral boundary and sea surface conditions were kept identical between all CWRF runs such that planetary forcing signals outside of the domain and oceans were precluded. Furthermore, soil temperature anomalies in the downstream regions are very weak and hardly penetrating below 20 cm (Fig. S3). In fact, significant high positive (>0.4) correlations occur between daily precipitation and soil moisture variations during summer when the former leads by 2–0 days, whereas they are insignificant reversely. Thus, soil moisture anomalies, although significant in some regions, are mainly the result (rather than the cause) of local precipitation changes. Therefore, the primary mechanism that keeps the long memory outside the TP forcing area is likely preserved in the atmospheric circulation anomalies as identified above. In particular, the altered SAH and ULJ circulation features are responsible for the summer temperature and precipitation changes in East China.

Note also that subtle differences exist between the SVD statistical analysis and the CWRF perturbed simulation. The SVD results show lag correlations between the spring near-surface TP heating and the summer precipitation in East China. In contrast, the model simulations capture the dynamic effects of the initial surface and subsurface soil temperature perturbations that persist in the subsequent months. If the perturbation had been stopped at the end of May, the summer temperature and precipitation anomalies simulated by CWRF would be truly delayed responses. However, as discussed above, the remaining TP perturbation after June tend to play a minor role on July–August anomalies over East China. Additional experiments may be helpful to confirm this argument.

6 Conclusion

Observational data analysis showed that spring surface air temperature anomalies on TP were correlated with summer precipitation variations in East China. Since CWRF reproduced well this observed relationship, it was used here for a case study in 2003 to explore the physical processes and underlying mechanisms of how initial TP soil heating in May induces significant local and remote responses in summer temperature and precipitation. We found that initial heat in deep soil layers is memorized for several months and continues to be transmitted upwards through the surface to the atmosphere from spring through summer. This provides an elevated heating source through longwave emission and sensible/latent heat flux to warm/moist the air and enhance local convection and precipitation. The enhanced moist convection causes larger condensation latent plus subsidence adiabatic heating to the mid-troposphere, in which the prevailing westerly advection and thermal expansion transport the heat downstream to produce widespread warming in the mid-upper troposphere beyond the forcing area over TP. This transport is accomplished through Rossby waves with significant vorticity anomalies induced by the TP heating. These waves are initially propagating downstream and eventually become stationary, causing important circulation anomalies over the ULJ exit region. Together, the warming strengthens the SAH and shifts the ULJ, which induces stronger

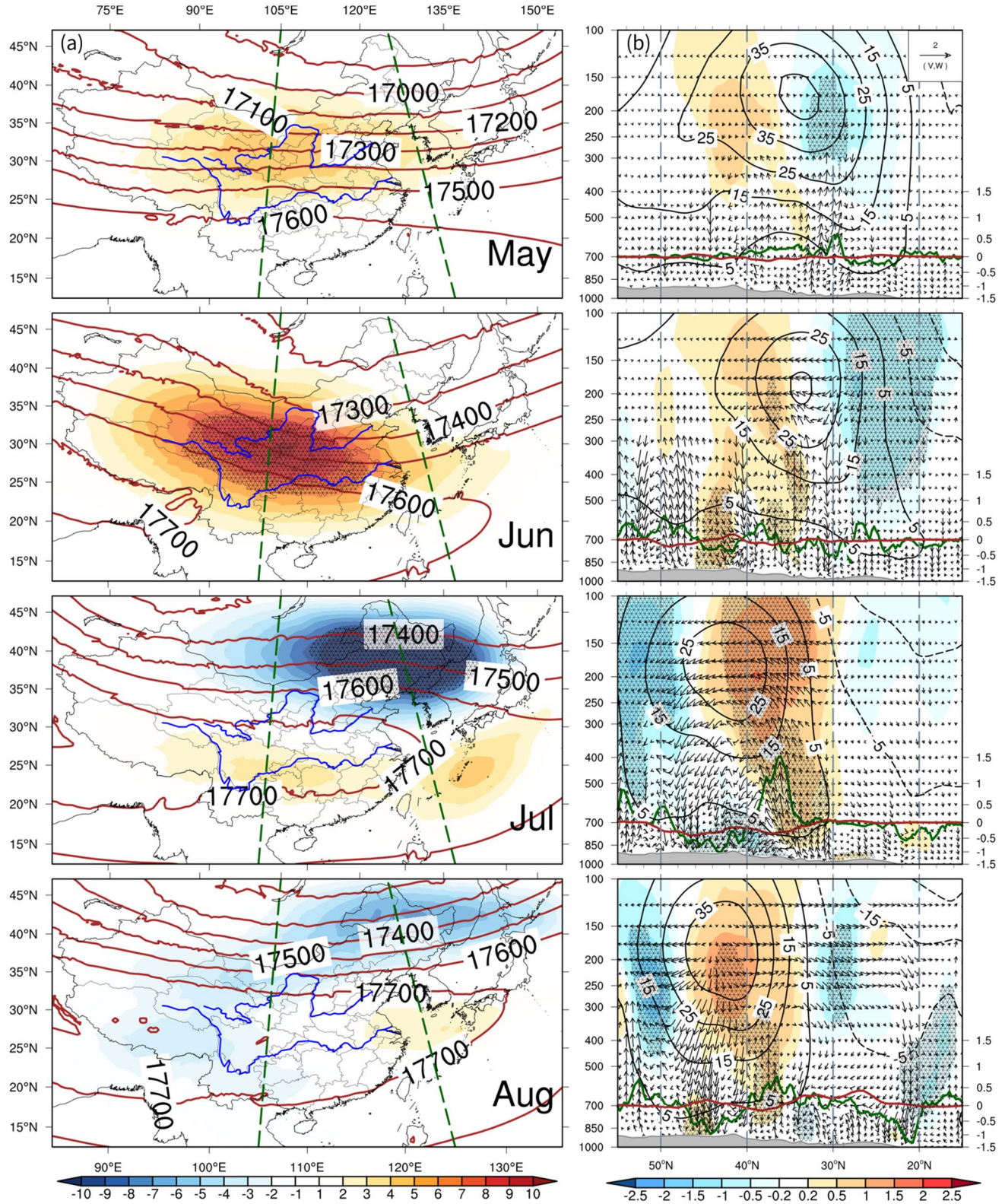

subsidence cooling air behind the jet left exit and ascending motions to the right. Consequently, in July, a south shift of the ULJ is accompanied by a significant cooling and drier center over the Northeast and a heavier rainfall center in North China. There are other responses in both temperature

◂**Fig. 9** CWRF simulated **a** monthly (May–August) mean differences between the warm start IbTpWc and IbTnWn in 100-hPa geopotential height (colors, m), overlaid with IbTnWn 100-hPa geopotential height (red contours, m), and 105° E and 125° E longitudes (green dash lines), and **b** altitude (pressure, hPa)-latitude cross section of the 105° E–125° E longitudinal mean wind circulation differences between the warm start IbTpWc and IbTnWn from May to August. In **b**, the zonal (m s^{-1}) and meridional (m s^{-1})/ vertical (10^{-4} hPa s^{-1}) wind components are represented by contours and vectors, respectively. The shaded areas denote the statistical significance at the $\alpha < 0.1$ level of *t* test values. The thick curves show the corresponding longitudinal mean precipitation (green, mm day^{-1}) and temperature (red, ºC) differences, and the gray shading depicts the mean terrain elevation

and precipitation over broad regions in East China, depending on which month from May to August.

Our results confirmed that the spring TP soil heating has an important delayed impact on downstream precipitation in East China. Two issues warrant further investigation. One issue is due to the extremely rare availability of observational data over TP. Currently, monitoring temperature and precipitation data are available only for a few sites in the central to western Tibet (see Fig. S1 in Liang et al. 2018), and soil temperature observations are even less (see Fig. S1 in Liu et al. 2020). The modern reanalyses also contain great uncertainties over TP (Xu et al. 2021), and correlations among different reanalyses are generally low. This makes it extremely difficult to evaluate the model performance or identify model biases for improving soil initialization. Another issue concerns the source of the spring TP thermal forcing, whether it is due to observed anomalies or model deficiencies. Some studies argued that anomalies in winter snowfall and subsequent snow accumulation change surface albedo and so solar radiation to impose thermal forcing from the surface into deep soil storage for later release in spring (Souma and Wang 2010; Lau and Kim 2018). Others showed that model radiation schemes have the greatest impact on TP temperature simulations (Xu et al. 2021). In both cases, the heating transfer from the surface to subsurface layers is a very slow process, still open to understand its actual role for charging the signal.

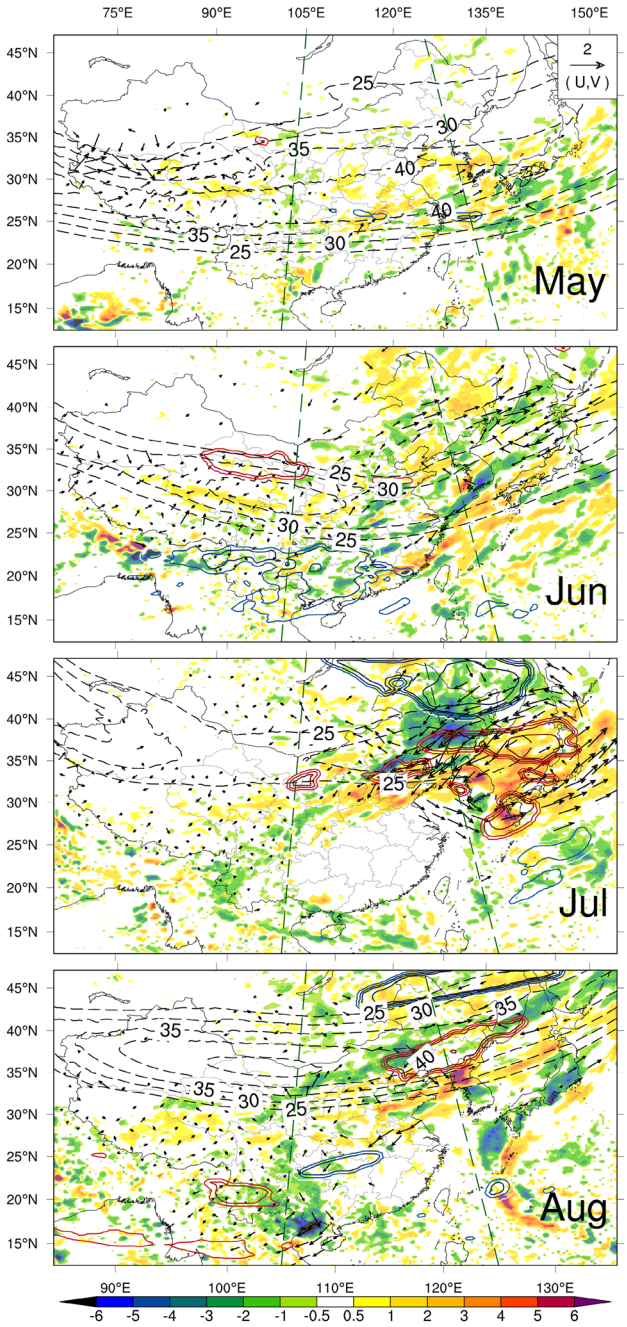

Fig. 10 CWRF simulated monthly (May–August) mean differences between the warm start IbTpWc and IbTnWn in 850-hPa horizontal wind (vector, m s^{-1}), 200-hPa zonal wind (contour, $\pm\{0.5, 1.0, 1.5\}$ m s^{-1}) and precipitation (color, mm day^{-1}), overlaid with IbTnWn 200-hPa zonal wind speeds in dashed contours (staring from 25 at an interval of 5)

Supplementary Information The online version contains supplementary material available at https://doi.org/10.1007/s00382-022-06266-5.

Acknowledgements The research was supported by the U.S. National Science Foundation Innovations at the Nexus of Food, Energy and Water Systems under Grant EAR1903249 and the China Meteorological Administration/National Climate Center research subcontract 2211011816501. The simulations and analyses were conducted on computers in the Maryland Advanced Research Computing Center and the National Center for Atmospheric Research Computational and Information Systems Lab.

Funding Prof. Xin-Zhong Liang have National Science Foundation (EAR1903249), China Meteorological Administration (2211011816501).

Data availability Observational data and model simulations used in this study are accessible online (ftp://earthserver.umd.edu/pub/TP_heating).

Declarations

Conflict of interest The authors declare that they have no conflict of interests.

References

Banzon V, Smith TM, Chin TM, Liu C, Hankins W (2016) A long-term record of blended satellite and in situ sea-surface temperature for climate monitoring, modeling and environmental studies. Earth Syst Sci Data 8:165–176. https://doi.org/10.5194/essd-8-165-2016

Bretherton CS, Park S (2009) A new moist turbulence parameterization in the Community Atmosphere Model. J Clim 22:3422–3448. https://doi.org/10.1175/2008jcli2556.1

Bretherton CS, Smith C, Wallace JM (1992) An intercomparison of methods for finding coupled patterns in climate data. J Clim 5:541–560

Chen S-C, Trenberth KE (1988) Orographically forced planetary waves in the Northern Hemisphere winter: steady state model with wave-coupled lower boundary formulation. J Atmos Sci 45:657–681

Chen L, Liang X-Z, DeWitt D, Samel AN, Wang JXL (2016) Simulation of seasonal US precipitation and temperature by the nested CWRF-ECHAM system. Clim Dyn 46:879–896. https://doi.org/10.1007/s00382-015-2619-9

Choi HI, Liang X-Z (2010) Improved terrestrial hydrologic representation in mesoscale land surface models. J Hydrometeorol 11:797–809. https://doi.org/10.1175/2010jhm1221.1

Choi HI, Kumar P, Liang X-Z (2007) Three-dimensional volume-averaged soil moisture transport model with a scalable parameterization of subgrid topographic variability. Water Resour Res. https://doi.org/10.1029/2006wr005134

Choi HI, Liang X-Z, Kumar P (2013) A conjunctive surface–subsurface flow representation for mesoscale land surface models. J Hydrometeorol 14:1421–1442. https://doi.org/10.1175/jhm-d-12-0168.1

Chou M-D, Suarez MJ (1999) A solar radiation parameterization for atmospheric studies. [Last revision on March 2002] Technical Report Series on Global Modeling and Data Assimilation. Suarez MJ (ed) NASA/TM-1999-104606, Vol. 15, Goddard Space Flight Center, Greenbelt, p 42

Chou M-D, Suarez MJ, Liang X-Z, Yan MM-H (2001) A thermal infrared radiation parameterization for atmospheric studies. [Last revision on July 2002] Technical Report Series on Global Modeling and Data Assimilation. Suarez MJ (ed) NASA/TM-2001-104606, Vol. 19, Goddard Space Flight Center, Greenbelt, p 56

Dee DP, Uppala SM, Simmons AJ, Berrisford P, Poli P, Kobayashi S, Andrae U, Balmaseda MA, Balsamo G, Bauer P, Bechtold P, Beljaars ACM, van de Berg L, Bidlot J, Bormann N, Delsol C, Dragani R, Fuentes M, Geer AJ, Haimberger L, Healy SB, Hersbach H, Hólm EV, Isaksen L, Kållberg P, Köhler M, Matricardi M, McNally AP, Monge-Sanz BM, Morcrette JJ, Park BK, Peubey C, de Rosnay P, Tavolato C, Thépaut JN, Vitart F (2011) The ERA-Interim reanalysis: configuration and performance of the data assimilation system. Quart J Meteorol Soc 137:553–597

Ding Y (1992) Summer monsoon rainfalls in China. J Meteorol Soc Japan Ser II 70:373–396. https://doi.org/10.2151/jmsj1965.70.1b_373

Ding L, Spicer RA, Yang J, Xu Q, Cai F, Li S, Lai Q, Wang H, Spicer TEV, Yue Y, Shukla A, Srivastava G, Khan MA, Bera S, Mehrotra R (2017) Quantifying the rise of the Himalaya orogen and implications for the South Asian monsoon. Geology 45:215–218. https://doi.org/10.1130/g38583.1

Frauenfeld OW, Zhang T, Serreze MC (2005) Climate change and variability using European Centre for Medium-Range Weather Forecasts reanalysis (ERA-40) temperatures on the Tibetan Plateau. J Geophys Res 110:D02101. https://doi.org/10.1029/2004jd005230

Gan Y, Liang X-Z, Duan Q, Choi H, Dai Y, Wu H (2015) Stepwise sensitivity analysis from qualitative to quantitative: application to the terrestrial hydrological modeling of a conjunctive surface-subsurface process (CSSP) land surface model. J Adv Model Earth Syst 7:648–669. https://doi.org/10.1002/2014ms000406

Gao H, Yang S (2009) A severe drought event in northern China in winter 2008–2009 and the possible influences of La Niña and Tibetan Plateau. J Geophys Res 114:D24104. https://doi.org/10.1029/2009jd012430

He H, McGinnis JW, Song Z, Yanai M (1987) Onset of the Asian summer monsoon in 1979 and the effect of the Tibetan Plateau. Mon Wea Rev 115:1966–1995

He J, Yang K, Tang W, Lu H, Qin J, Chen Y, Li X (2020) The first high-resolution meteorological forcing dataset for land process studies over China. Sci Data 7:1–11. https://doi.org/10.1038/s41597-020-0369-y

Holtslag AAM, Boville BA (1993) Local versus nonlocal boundary-layer diffusion in a global climate model. J Clim 6:1825–1842

Hoskins BJ, Karoly DJ (1981) The steady linear response of a spherical atmosphere to thermal and orographic forcing. J Atmos Sci 38:1179–1196

Hsu H-H, Liu X (2003) Relationship between the Tibetan Plateau heating and East Asian summer monsoon rainfall. Geophys Res Lett 30:2066. https://doi.org/10.1029/2003gl017909

Hu Q, Feng S (2004) A role of the soil enthalpy in land memory. J Clim 17:3633–3643

Huang R, Chen J, Huang G (2007) Characteristics and variations of the East Asian monsoon system and its impacts on climate disasters in China. Adv Atmos Sci 24:993–1023. https://doi.org/10.1007/s00376-007-0993-x

Ji P, Yuan X, Liang X-Z (2017) Do lateral flows matter for the hyperresolution land surface modeling? J Geophys Res Atmos 122:12077–12092. https://doi.org/10.1002/2017jd027366

Jiang R, Sun L, Sun C, Liang X-Z (2021) CWRF downscaling and understanding of China precipitation projections. Clim Dyn. https://doi.org/10.1007/s00382-021-05759-z

Kahn RA, Gaitley BJ, Martonchik JV, Diner DJ, Crean KA, Holben B (2005) Multiangle Imaging Spectroradiometer (MISR) global

aerosol optical depth validation based on 2 years of coincident aerosol robotic network (AERONET) observations. J Geophys Res 110:D10S04. https://doi.org/10.1029/2004JD004706
Kong W, Chiang JCH (2020) Interaction of the westerlies with the Tibetan Plateau in determining the mei-yu termination. J Clim 33:339–363. https://doi.org/10.1175/jcli-d-19-0319.1
Lau W, Kim K-M (2018) Impact of snow darkening by deposition of light-absorbing aerosols on snow cover in the Himalayas-Tibetan Plateau and influence on the Asian Summer Monsoon: a possible mechanism for the Blanford hypothesis. Atmosphere 9:438. https://doi.org/10.3390/atmos9110438
Li W, Guo W, Qiu B, Xue Y, Pang-Chi Hsu P-C, Wei J (2018) Influence of Tibetan Plateau snow cover on East Asian atmospheric circulation at medium-range time scales. Nat Commun 9:4243. https://doi.org/10.1038/s41467-018-06762-5
Li Q, Wang T, Wang F, Liang X-Z, Zhao C, Dong L, Zhao C, Xie B (2020) Dynamical downscaling simulation of the East Asian summer monsoon in a regional climate-weather research and forecasting model. Int J Climatol 41:E1700–E1716. https://doi.org/10.1002/joc.6800
Liang X-Z, Wang WC (1998) Associations between China monsoon rainfall and tropospheric jets. Q J R Meteorol Soc. https://doi.org/10.1256/smsqj.55203
Liang X-Z, Zhang F (2013) The cloud-aerosol-radiation (CAR) ensemble modeling system. Atmos Chem Phys 13:8335–8364. https://doi.org/10.5194/acp-13-8335-2013
Liang X-Z, Samel AN, Wang W-C (1995) Observed and GCM simulated decadal variability of monsoon rainfall in east China. Clim Dyn 11:103–114
Liang X-Z, Li L, Dai A, Kunkel KE (2004a) Regional climate model simulation of summer precipitation diurnal cycle over the United States. Geophys Res Lett 31:L24208. https://doi.org/10.1029/2004GL021054
Liang X-Z, Li L, Kunkel KE, Ting M, Wang JXL (2004b) Regional climate model simulation of US precipitation during 1982–2002. Part 1: annual cycle. J Clim 17:3510–3528
Liang X-Z, Choi H, Kunkel KE, Dai Y, Joseph E, Wang JXL, Kumar P (2005a) Surface boundary conditions for mesoscale regional climate models. Earth Interact 9:1–28. https://doi.org/10.1175/ei151.1
Liang X-Z, Xu M, Gao W, Kunkel K, Slusser J, Dai Y, Min Q, Houser PR, Rodell M, Schaaf CB, Gao F (2005b) Development of land surface albedo parameterization based on moderate resolution imaging spectroradiometer (MODIS) data. J Geophys Res 110:D11107. https://doi.org/10.1029/2004jd005579
Liang X-Z, Xu M, Choi HI, Kunkel KE, Rontu L, Geleyn J-F, Müller MD, Joseph E, Wang JXL (2006) Development of the regional Climate-Weather Research and Forecasting model (CWRF): treatment of subgrid topography effects. In: Proceedings of the 7th annual WRF user's workshop, Boulder, June 19–22, p 5
Liang X-Z, Xu M, Yuan X, Ling T, Choi HI, Zhang F, Chen L, Liu S, Su S, Qiao F, He Y, Wang JXL, Kunkel KE, Gao W, Joseph E, Morris V, Yu T-W, Dudhia J, Michalakes J (2012) Regional climate-weather research and forecasting model (CWRF). Bull Am Meteorol Soc 93:1363–1387. https://doi.org/10.1175/bams-d-11-00180.1
Liang X-Z, Sun C, Zheng X, Dai Y, Xu M, Choi HI, Ling T, Qiao F, Kong X, Bi X, Song L, Wang F (2018) CWRF performance at downscaling China climate characteristics. Clim Dyn 52:2159–2184. https://doi.org/10.1007/s00382-018-4257-5
Ling T-J, Liang X-Z, Xu M, Wang Z, Wang B (2011) A multilevel ocean mixed-layer model for 2-dimension applications. Acta Oceanol Sin 33(03):1–10
Ling T-J, Xu M, Liang X-Z, Wang JXL, Noh Y (2015) A multilevel ocean mixed layer model resolving the diurnal cycle: Development and validation. J Adv Model Earth Syst 7:1680–1692. https://doi.org/10.1002/2015ms000476
Liu X, Yanai M (2002) Influence of Eurasian spring snow cover on Asian summer rainfall. Int J Climatol 22:1075–1089. https://doi.org/10.1002/joc.784
Liu H, Sun Z, Wang J, Min J (2004) A modeling study of the effects of anomalous snow cover over the Tibetan Plateau upon the South Asian summer monsoon. Adv Atmos Sci 21:964–975. https://doi.org/10.1007/bf02915598
Liu S, Liang X-Z, Gao W, Zhang H (2008) Climate-weather research and forecasting model (CWRF) application in China: domain optimization. Chin J Atmos Sci 32:457–468. https://doi.org/10.3878/j.issn.1006-9895.2008.03.04
Liu B, Wu G, Mao J, He J (2013) Genesis of the South Asian high and its impact on the Asian summer monsoon onset. J Clim 26:2976–2991. https://doi.org/10.1175/jcli-d-12-00286.1
Liu S, Wang JXL, Liang X-Z, Morris V, Fine SS (2016) A hybrid approach to improve US seasonal climate outlook skills at the regional scale. Clim Dyn 46:483–494. https://doi.org/10.1007/s00382-015-2594-1
Liu Y, Xue Y, Li Q, Lettenmaier D, Zhao P (2020) Investigation of the variability of near-surface temperature anomaly and its causes over the Tibetan Plateau. J Geophys Res Atmos 125:e2020JD032800. https://doi.org/10.1029/2020JD032800
Luo S, Qian Z, Wang Q (1982) The climatic and synoptical study about the relation between the Qinghai-Xizang high pressure on the 100mb surface and the flood and drought in East China in summer. Plateau Meteor 1:3–12 (**in Chinese**)
Qian YF, Zheng YQ, Zhang Y, Miao MQ (2003) Responses of China's summer monsoon climate to snow anomaly over the Tibetan Plateau. Int J Climatol 23:593–613. https://doi.org/10.1002/joc.901
Qiao F, Liang X-Z (2015) Effects of cumulus parameterizations on predictions of summer flood in the Central United States. Clim Dyn 45:727–744. https://doi.org/10.1007/s00382-014-2301-7
Qiao F, Liang X-Z (2016) Effects of cumulus parameterization closures on simulations of summer precipitation over the United States coastal oceans. J Adv Model Earth Syst 8:764–785. https://doi.org/10.1002/2015ms000621
Qiao F, Liang X-Z (2017) Effects of cumulus parameterization closures on simulations of summer precipitation over the continental United States. Clim Dyn 49:225–247. https://doi.org/10.1007/s00382-016-3338-6
Ren X, Yang D, Yang X-Q (2015) Characteristics and mechanisms of the subseasonal eastward extension of the South Asian high. J Clim 28:6799–6822. https://doi.org/10.1175/jcli-d-14-00682.1
Reynolds RW, Smith TM, Liu C, Chelton DB, Casey KS, Schlax MG (2007) Daily high-resolution-blended analyses for sea surface temperature. J Clim 20:5473–5496. https://doi.org/10.1175/2007jcli1824.1
Riyu L (2000) Anomalies in the tropics associated with the heavy rainfall in east asia during the summer of 1998. Adv Atmos Sci 17:205–220. https://doi.org/10.1007/s00376-000-0004-y
Rontu L (2006) A study on parameterization of orography-relate momentum fluxes in a synoptic-scale NWP model. Tellus A 58:69–81. https://doi.org/10.1111/j.1600-0870.2006.00162.x
Samel AN, Wang W-C, Liang X-Z (1999) The monsoon rainband over China and relationships with the Eurasian circulation. J Clim 12:115–131. https://doi.org/10.1175/1520-0442-12.1.115
Seol K-H, Hong S-Y (2009) Relationship between the Tibetan snow in spring and the East Asian summer monsoon in 2003: a global and regional modeling study. J Clim 22:2095–2110. https://doi.org/10.1175/2008jcli2496.1
Shi W, Chen H, Liang X-Z (2021) CWRF-based ensemble simulation of tropical cyclone activity near China and its sensitivity to the model physical parameterization schemes. Atmos Oceanic Sci Lett 14:100004. https://doi.org/10.1016/j.aosl.2020.100004

Skamarock WC, Klemp JB, Dudhia J, Gill DO, Barker DM, Duda MG,Huang X-Y, Wang W, Powers JG (2008) A description of the advanced research WRF Version 3. NCAR Technical, Boulder, (Note, NCAR/TN-475 + STR), p 113

Souma K, Wang Y (2010) A comparison between the effects of snow albedo and infiltration of melting water of Eurasian snow on East Asian summer monsoon rainfall. J Geophys Res Atmos. https://doi.org/10.1029/2009jd012189

Sun L, Liang X-Z, Ling T, Xu M, Lee X (2020a) Improving a multilevel turbulence closure model for a shallow lake in comparison with other 1-D models. J Adv Model Earth Syst 12:e2019MS001971. https://doi.org/10.1029/2019ms001971

Sun L, Liang X-Z, Xia M (2020b) Developing the coupled CWRF-FVCOM modeling system to understand and predict atmosphere-watershed interactions over the Great Lakes Region. J Adv Model Earth Syst 12:e2020MS002319. https://doi.org/10.1029/2020ms002319

Tao S, Zhu F (1964) The 100mb flow patterns in Southern Asia in summer and its relation to the advance and retreat of the west-pacific Subtropical anticyclone over the Far East. Acta Meteorol Sin 34:387–396. https://doi.org/10.11676/qxxb1964.039 (**in Chinese**)

Tao W-K, Simpson J, Baker D, Braun S, Chou M-D, Ferrier B, Johnson D, Khain A, Lang S, Lynn B, Shie C-L, Starr D, Sui C-H, Wang Y, Wetzel P (2003) Microphysics, radiation and surface processes in the Goddard Cumulus Ensemble (GCE) model. Meteorol Atmos Phys 82:97–137

Ueda H, Yasunari T (1998) Role of warming over the Tibetan Plateau in early onset of the summer monsoon over the Bay of Bengal and the South China Sea. J Meteorol Soc Japan Ser II 76:1–12. https://doi.org/10.2151/jmsj1965.76.1_1

Wan B, Gao Z, Chen F, Lu C (2017) Impact of Tibetan Plateau surface heating on persistent extreme precipitation events in southeastern China. Mon Wea Rev 145:3485–3505. https://doi.org/10.1175/mwr-d-17-0061.1

Wang A, Zeng X (2012) Evaluation of multireanalysis products with in situ observations over the Tibetan Plateau. J Geophys Res 117:D05102. https://doi.org/10.1029/2011jd016553

Wang Z, Yang S, Lau N-C, Duan A (2018) Teleconnection between summer NAO and East China rainfall variations: a bridge effect of the Tibetan Plateau. J Clim 31:6433–6444. https://doi.org/10.1175/jcli-d-17-0413.1

Wei W, Zhang R, Wen M, Kim B-J, Nam J-C (2015) Interannual variation of the South Asian high and its relation with Indian and East Asian summer monsoon rainfall. J Clim 28:2623–2634. https://doi.org/10.1175/jcli-d-14-00454.1

Wei J, Zhao J, Chen H, Liang X-Z (2021) Coupling between land surface fluxes and lifting condensation level: mechanisms and sensitivity to model physics parameterizations. J Geophys Res Atmos. https://doi.org/10.1029/2020jd034313

Wu G-X (1984) The nonlinear response of the atmosphere to large-scale mechanical and thermal forcing. J Atmos Sci 41:2456–2476

Wu T-W, Qian Z-A (2003) The relation between the Tibetan winter snow and the Asian summer monsoon and rainfall: an observational investigation. J Clim 16:2038–2051

Wu G-X, Duan A, Liu Y, Mao J, Ren R, Bao Q, He B, Liu B, Hu W (2014) Tibetan Plateau climate dynamics: recent research progress and outlook. Natl Sci Rev 2:100–116. https://doi.org/10.1093/nsr/nwu045

Xiao Z, Duan A (2016) Impacts of Tibetan Plateau snow cover on the interannual variability of the East Asian summer monsoon. J Clim 29:8495–8514. https://doi.org/10.1175/jcli-d-16-0029.1

Xie A, Ren J, Qin X, Kang S (2007) Reliability of NCEP/NCAR reanalysis data in the Himalayas/Tibetan Plateau. J Geogr Sci 17:421–430. https://doi.org/10.1007/s11442-007-0421-2

Xu K-M, Randall DA (1996) A semiempirical cloudiness parameterization for use in climate models. J Atmos Sci 53:3084–3102

Xu M, Liang X-Z, Samel A, Gao W (2014) MODIS consistent vegetation parameter specifications and their impacts on regional climate simulations. J Clim 27:8578–8596. https://doi.org/10.1175/jcli-d-14-00082.1

Xu R, Liang X-Z, Duan M (2021) Evaluation of CWRF simulation of temperature and precipitation on the Qinghai-Tibet Plateau. Trans Atmos Sci 44:104–117 (**in Chinese**)

Xue Y, Vasic R, Janjic Z, Liu YM, Chu PC (2012) The impact of spring subsurface soil temperature anomaly in the western U.S. on North American summer precipitation: a case study using regional climate model downscaling. J Geophys Res 117:D11103. https://doi.org/10.1029/2012jd017692

Xue Y, Diallo I, Li W, David Neelin J, Chu PC, Vasic R, Guo W, Li Q, Robinson DA, Zhu Y, Fu C, Oaida CM (2018) Spring land surface and subsurface temperature anomalies and subsequent downstream late spring-summer droughts/floods in North America and East Asia. J Geophys Res 123:5001–5019. https://doi.org/10.1029/2017jd028246

Xue Y, Yao T, Boone AA, Diallo I, Liu Y, Zeng X, Lau WKM, Sugimoto S, Tang Q, Pan X, van Oevelen PJ, Klocke D, Koo M-S, Sato T, Lin Z, Takaya Y, Ardilouze C, Materia S, Saha SK, Senan R, Nakamura T, Wang H, Yang J, Zhang H, Zhao M, Liang X-Z, Neelin JD, Vitart F, Li X, Zhao P, Shi C, Guo W, Tang J, Yu M, Qian Y, Shen SSP, Zhang Y, Yang K, Leung R, Qiu Y, Peano D, Qi X, Zhan Y, Brunke MA, Chou SC, Ek M, Fan T, Guan H, Lin H, Liang S, Wei H, Xie S, Xu H, Li W, Shi X, Nobre P, Pan Y, Qin Y, Dozier J, Ferguson CR, Balsamo G, Bao Q, Feng J, Hong J, Hong S, Huang H, Ji D, Ji Z, Kang S, Lin Y, Liu W, Muncaster R, de Rosnay P, Takahashi HG, Wang G, Wang S, Wang W, Zhou X, Zhu Y (2021) Impact of initialized land surface temperature and snowpack on subseasonal to seasonal prediction project, phase I (LS4P-I): organization and experimental design. Geosci Model Dev 14:4465–4494. https://doi.org/10.5194/gmd-14-4465-2021

Yanai M, Li C, Song Z (1992) Seasonal heating of the Tibetan Plateau and its effects on the evolution of the Asian summer monsoon. J Meteorol Soc Japan 70:319–351

Yang K, Zhang J (2015) Spatiotemporal characteristics of soil temperature memory in China from observation. Theor Appl Climatol 126:739–749. https://doi.org/10.1007/s00704-015-1613-9

Ye D (1981) Some characteristics of the summer circulation over the Qinghai-Xizang (Tibet) Plateau and its neighborhood. Bull Am Meteorol Soc 62:14–19

You Q, Fraedrich K, Ren G et al (2013) Variability of temperature in the Tibetan Plateau based on homogenized surface stations and reanalysis data. Int J Climatol 33:1337–1347. https://doi.org/10.1002/joc.3512

You Q, Min J, Kang S (2016) Rapid warming in the Tibetan Plateau from observations and CMIP5 models in recent decades. Int J Climatol 36:2660–2670. https://doi.org/10.1002/joc.4520

You Q, Wu T, Shen L, Pepin N, Zhang L, Jiang Z, Wu Z, Kang S, AghaKouchak A (2020) Review of snow cover variation over the Tibetan Plateau and its influence on the broad climate system. Earth Sci Rev. https://doi.org/10.1016/j.earscirev.2019.103043

Yuan X, Liang X-Z (2011a) Evaluation of a conjunctive surface-subsurface process model (CSSP) over the contiguous United States at regional–local scales. J Hydrometeorol 12:579–599. https://doi.org/10.1175/2010jhm1302.1

Yuan X, Liang X-Z (2011b) Improving cold season precipitation prediction by the nested CWRF-CFS system. Geophys Res Lett 38:L02706. https://doi.org/10.1029/2010gl046104

Yuan X, Ji P, Wang L, Liang X-Z, Yang K, Ye A, Su Z, Wen J (2018) High-resolution land surface modeling of hydrological changes over the Sanjiangyuan region in the eastern Tibetan Plateau: 1.

Model development and evaluation. J Adv Model Earth Syst 10:2806–2828. https://doi.org/10.1029/2018ms001412

Zeng Q-C, Liang X-Z, Zhang M-H (1988) Numerical simulation of monsoons and the abrupt seasonal changing of atmospheric general circulation. Chin J Atmos Sci, special issue :22–42 **(in Chinese)**

Zhang L, Zhou T (2015) Drought over East Asia: a review. J Clim 28:3375–3399. https://doi.org/10.1175/jcli-d-14-00259.1

Zhang Y, Li T, Wang B (2004) Decadal change of the spring snow depth over the Tibetan Plateau: the associated circulation and influence on the East Asian summer monsoon. J Clim 17:2780–2793

Zhang P, Song Y, Vernon EK (2005) South Asian high and Asian-Pacific-American climate teleconnection. Adv Atmos Sci 22:915–923. https://doi.org/10.1007/bf02918690

Zhang F, Liang X-Z, Li J, Zeng Q (2013) Dominant roles of subgridscale cloud structures in model diversity of cloud radiative effects. J Geophys Res 118:7733–7749

Zhao P, Zhou Z, Liu J (2007) Variability of Tibetan spring snow and its associations with the hemispheric extratropical circulation and East Asian summer monsoon rainfall: an observational investigation. J Clim 20:3942–3955. https://doi.org/10.1175/jcli4205.1

Zhao P, Xu X, Chen F, Guo X, Zheng X, Liu L, Hong Y, Li Y, La Z, Peng H, Zhong L, Ma Y, Tang S, Liu Y, Liu H, Li Y, Zhang Q, Hu Z, Sun J, Zhang S (2018) The third atmospheric scientific experiment for understanding the Earth–atmosphere coupled system over the Tibetan Plateau and its effects. Bull Am Meteorol Soc 99:757–776. https://doi.org/10.1175/bams-d-16-0050.1

Zhu Y-Y, Yang S (2020) Evaluation of CMIP6 for historical temperature and precipitation over the Tibetan Plateau and its comparison with CMIP5. Adv Clim Change Res 11:239–251. https://doi.org/10.1016/j.accre.2020.08.001